Journal of Alloys and Compounds 928 (2022) 167112

Contents lists available at ScienceDirect

Journal of Alloys and Compounds

journal homepage: www.elsevier.com/locate/jalcom

Research article

Development of a non-equimolar AlCrCuFeNi high-entropy alloy and its corrosive response to marine environment under different temperatures and chloride concentrations

L. Xue[a,b], Y. Ding[b], K.G. Pradeep[c], R. Case[b], H. Castaneda[b], M. Paredes[a,*]

[a] Ocean Engineering Department, Texas A&M University, Galveston TX 77554, USA
[b] National Corrosion and Materials Reliability Laboratory, Texas A&M University, College Station TX 77840, USA
[c] Department of Metallurgical and Materials Engineering, Indian Institute of Technology Madras, Chennai 600036, India

ARTICLE INFO

Article history:
Received 6 July 2022
Received in revised form 31 August 2022
Accepted 4 September 2022
Available online 9 September 2022

Keywords:
High-entropy alloys
Electrochemical analysis
Passive film
Localized corrosion
Point Defect Model

ABSTRACT

This work aims to characterize the influence of temperature and chloride solution concentration on the corrosion behavior of a newly developed high-entropy alloy system ($Al_2Cr_5Cu_5Fe_{53}Ni_{35}$) in a simulated marine environment. A direct correlation was found between temperature and chloride concentration with localized corrosion resistance. The Point Defect Model approach is employed to analyze the influence of the temperature and chloride concentration upon the properties of the passive film formation over the alloy surface in seawater solutions. It turns out that the present system alloy exhibits a better local corrosion resistance than conventional martensitic stainless steel UNS S40300 when temperature is below 60 °C in similar electrolytic environment.

1. Introduction

A newly discovered advanced alloys known as high-entropy alloys (HEAs) have attracted research interest in the past two decades. The high-entropy alloys, more generally referred to as complex-concentrated alloys (CCAs), contain five or more principal elements in equimolar ratios were firstly proposed by Cantor et al. [1] and Yeh et al. [2–5,6] independently in 2004. When first introduced, HEAs were defined as, "those compounds of five or more principal elements in equimolar ratios" [2]. However, in the same reference, the authors claimed that a relaxation of the equimolar restriction is possible, hence a new interesting configurational space can be unveiled. Nowadays, the HEAs are expanded to include, "multi-principal elements with concentrations between 5 and 35 at.-%". Some HEAs might conveniently contain minor amount of elements in order to obtain certain specific mechanical properties and microstructure configurations [7].

Owing to the extremely broad ranges of compositions and microstructures of HEAs, new physical phenomena and exceptional properties have being reported. For instance, the dual FCC phase CoCuFeMnNi wire exhibited extraordinary high strength (2 GPa) at room temperature [8]; whereas CrCoNi reported exceptional damage-tolerance at cryogenic temperatures [9] as well as a new strengthening mechanism, called magnetic hardening, was recently discovered in the same configuration [10]. Likewise, the non-equiatomic $Fe_{80x}Mn_xCo_{10}Cr_{10}$ HEA system combines increasing strength and ductility by overcoming the strength–ductility trade-off through promoting metastable dual-phase formation and transformation induced plasticity mechanism (TRIP-DP-HEA) [11]. Due to the appealing properties of these newly discovered alloys, HEAs are shaping the future of material design and manufacturing [7,12,13]. Since the first single-phase, solid solution, high-entropy alloy AlCoCrFeNi, reported by Yeh et al. [2], a staggering number of research studies have been published over the years about different systems being the most relevant the $Al_xCoCrFeNi$ alloys. The mechanical properties of HEAs have also been one of the most relevant research topics [7,14–16] in parallel with the corrosion-resistant studies since environmentally assisted cracking problem still remains unchallenged [17–20,21]. HEAs are expected to be corrosion-resistant materials because of the presence of some passivating elements, like Cr, Ni, Mo, etc. in the matrix. Experimental results have revealed that cobalt (Co) is not necessarily essential for obtaining a single-phase, solid solution for high-entropy alloys [22], which can be fully substituted by nickel (Ni) to maintain similar level of face-centered

* Corresponding author.
E-mail address: lparedes@tamu.edu (M. Paredes).

https://doi.org/10.1016/j.jallcom.2022.167112
0925-8388/

cubic (FCC) single-phase, solid solution [23]. The copper (Cu) content might decreases the corrosion-resistance of the alloy [24], however, its presence has been revealed to be necessary for phase stabilization and precipitation formation of the ordered $L1_2$ (γ') phase in AlCrCuFeNi systems [25]. Likewise, Al content is known to enhance not only the strength, but also ductility of the alloy at the expense of its anticorrosive characteristics [20], hence the new HEA's selected configuration is based on the following elemental concentrations given in wt%: $Al_2Cr_5Cu_5Fe_{53}Ni_{35}$.

The metallic alloys' corrosion features are determined by the interactions between the material and environment. The common service environment in aqueous conditions for marine applications includes seawater, as well as acidic environments. In stainless steel, which is usually began with localized pitting rather than generalized surface corrosion. A clear example of local attack mechanism on stainless steel alloy is the influence of $M_{23}C_6$ and/or σ phases on the local formation of microcells resulting in Cr-depleted areas, which lead to local material dissolution [26,27]. Similar to stainless steels, the proposed high-entropy alloy system $Al_2Cr_5Cu_5Fe_{53}Ni_{35}$ is expected to have promising corrosion behavior in seawater due to the inclusion of passivating elements such as Cr and Ni in its composition. Like other traditional-corrosion resistant alloys, the above proposed HEA is assumed to form a protective passive film due to their passive properties of the selected elements. It can, nevertheless, undergo localized pitting corrosion, which is considered to be a major threat compared to uniform corrosion as structural failure is generally triggered by local mechanisms (nucleation and growth of pits). Moreover, the localized corrosion is more difficult to detect, predict and design against [28].

In the present work, to investigate the effect of the temperature and chloride solution concentration on the active-passive interfacial characteristics of the material, potentiodynamic-polarization and potentiostatic staircase tests were conducted at different temperatures and seawater concentrations. Comprehensive microstructural characterizations, such as x-ray diffraction (XRD), scanning electron microscopy (SEM), energy-dispersive spectrometer (EDS), and electron-backscattered diffraction (EBSD), were used to determine the microstructure of this new type HEA. Further, potentiostatic staircase method [29] was used to establish the potential formation and stability of pitting. The use of electrochemical impedance spectroscopy (EIS) and x-ray photoelectron spectroscopy (XPS) enable the analysis of the characteristics of the corrosion by-products (oxide film) during the passivation state. In addition, the experimental data were validated with the point defect model (PDM) [30–32], which can predict the pitting potential at different chloride solution concentrations and scan-rates. In order to understand the applicability of this novel high-entropy alloy, a direct comparison, via PDM, was performed with published results of conventional martensitic stainless steel . By revealing the microstructure and the corrosion behavior of the $Al_2Cr_5Cu_5Fe_{53}Ni_{35}$ in a seawater environment through complementary experiments, the present investigation is envisaged to provide additional understanding of the relationship between the corrosion properties of this new HEA system and its microstructure, thus providing useful information for potential structural alloys design for offshore applications.

2. Material and experimental methods

2.1. Test material

Using high-purity elemental constituents (such as Al, Cr, Cu, Fe, and Ni at 99.99 wt%) a $Al_2Cr_5Cu_5Fe_{53}Ni_{35}$ HEA system was synthesized via induction-melting. The as-cast rectangular ingots were then hot rolled at 900°C to 40% thickness reduction and were solution treated at 1200°C for 2 h in Ar atmosphere, followed by water quenching to eliminate as-cast microstructural heterogeneities. The dimension of the ingot is 5.6 inch × 12 inch × 0.5 inch (142.2 mm × 304.8 mm × 12.7 mm). Table 1 lists the chemical compositions of the HEA used in the current study. The samples for the microstructural characterization with SEM were cut into rectangular cuboids of 10 mm × 10 mm × 3 mm; then, they were wet polished with a series of SiC papers ranging from 200 to 1200 grit number to finally be mechanically polished using 3 μm, 1 μm and 0.04 μm diamond suspensions. For the EBSD samples, after being mechanically polished up to 0.04 μm, the samples were further vibrationally polished by employing 0.04 μm diamond suspension to remove the polishing scratches, then cleaned with alcohol before drying with nitrogen. The specimens for the electrochemical tests were machined as cylinders with a radius of 3 mm and a height of 43 mm. Prior to each electrochemical experiment, the exposed area (600 mm^2) of the specimens was wet grounded with SiC papers up to 1200 grit number, cleaned with alcohol, and then dried. Moreover, to study the passive film formation, the polished cubic samples were immersed in simulated seawater at room temperature (20 ± 2°C) for 21 days.

Table 1
Chemical compositions (at%) of $Al_2Cr_5Cu_5Fe_{53}Ni_{35}$ alloys.

Elements	Al	Cu	Cr	Fe	Ni
at%	1.87	5.16	5.12	52.22	35.63
EDS result (at%)	1.98	4.83	5.34	53.89	33.96

2.2. Microstructure characterization

The crystal structure of the $Al_2Cr_5Cu_5Fe_{53}Ni_{35}$ was characterized using XRD apparatus (Bruker D8 Discover). The sample was placed in a holder within a radiation-safe goniometer enclosure aligned with a laser-source video camera. The x-ray source was a 3 kW Cu x-ray tube maintained at an operating current of 40 kV and 40 mA (the wavelength is 1.54060 Å). The diffraction angle, 2θ, is defined between the incident beam and the detector. The incident angle ω is 1/2 of the detector angle 2θ. The 250 mm diameter $\theta - 2\theta$ goniometer was computer controlled with independent stepper motors and optical encoders for the θ circle with the angular step size of 0.005^o. The SEM and EBSD analyses were carried out using a Tescan FERA-3 Model GMH Focused Ion Beam Microscope. The concentration of elements in various phases was measured by EDS linked to the SEM system.

2.3. Electrochemical measurements

The electrochemical tests were conducted using a high-performance potentiostat workstation GAMRY Reference 600 + in a three-electrode electrochemical cell. The three-electrode cell consists of a tungsten/tungsten oxide reference electrode, a platinum mesh as auxiliary electrode, and a cylindrical HEA sample as the working electrode. The potentiodynamic-polarization measurements were conducted at six temperatures (2°C, 10°C, 25°C, 50°C, 60°C, and 75°C) under three different chloride solution concentrations. The PolyScience LM62GY1A110E LM6 Benchtop Chiller was used to control the temperature of the solution at 2°C, 10°C and 25°C. For higher temperatures, the Julabo C-B Series Open Heating Bath Circulator was employed to control the electrolyte temperature. The electrolytes were prepared containing inorganic salts in proportions and concentrations representative of seawater [33], then diluted to 10% chloride-containing solution and condensed to ten times chloride concentration in the solutions in order to obtain different chloride concentration electrolytes. The samples were left immersed in the solution overnight in order to reach a quasi-stationary value of the open circuit potential (OCP), which was initially applied before

Table 2
Sequence of experimental conditions used in the present study.

Chloride solution	0.1 × seawater																	
Temperature (°C)	2			10			25			50			60			75		
Scan rates (mV/s)	0.1	1	10	0.1	1	10	0.1	1	10	0.1	1	10	0.1	1	10	0.1	1	10
Chloride solution	1 × seawater																	
Temperature (°C)	2			10			25			50			60			75		
Scan rates (mV/s)	0.1	1	10	0.1	1	10	0.1	1	10	0.1	1	10	0.1	1	10	0.1	1	10
Chloride solution	10 × seawater																	
Temperature (°C)	2			10			25			50			60			75		
Scan rates (mV/s)	0.1	1	10	0.1	1	10	0.1	1	10	0.1	1	10	0.1	1	10	0.1	1	10

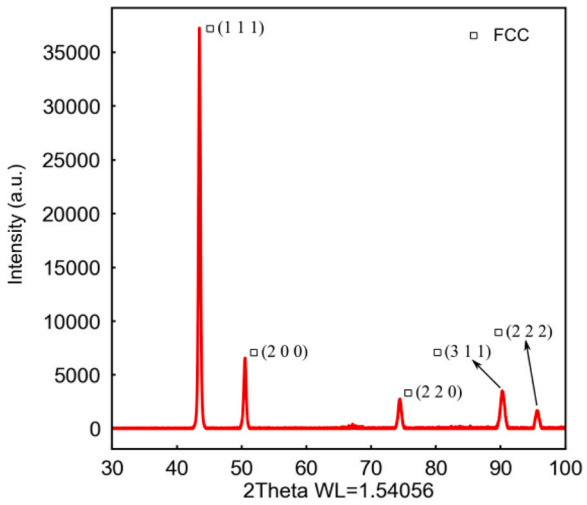

Fig. 1. X-ray diffraction patterns of $Al_2Cr_5Cu_5Fe_{53}Ni_{35}$ alloys.

each experiment begins. This is done to eliminate any electroactive species in the form of oxide that can alter the metal-electrolyte interface [34]. The potentiodynamic-polarization tests were performed at three different scan-rate (0.1 mV/s, 1 mV/s, and 10 mV/s), from an initial potential of − 0.4 V vs. OCP until either the potential exceeds the pitting potential or the current density reaches a maximum of 1 mA/cm^2. The adopted matrix analysis is summarized in Table 2 and covers for a wide range of temperatures, scan rates and seawater densities. The values of the electrochemical potential vs. the W/W_{oxide} reference electrode obtained from the tests were converted to potential vs. saturated calomel electrode (SCE) [35]. In order to confirm data reproducibility, each polarization test was performed at least three times. The potentiostatic bias step was set at 50 mV interval from the OCP until the current density exceeds 0.2 mA/cm^2. The potential is kept constant for 2 h at each step. Likewise, the EIS experiments were carried out at the OCP with a sinusoidal potential amplitude of 10 mV, running from 10 kHz to 10 mHz.

2.4. Identifying the corrosion products

The x-ray photoelectron spectroscopy was carried out by means Omicron XPS system with Argus detector. A Mg/Al X-ray source was employed to analyze the composition of the passive film formed on the surface samples. The spot size is 0.311 mm × 3.22 mm, and the pressure in the analysis chamber is 5×10^{-8} mbar. The spectral behavior were subsequently peak-fitted through CasaXPS software. In order to determine the morphologies of the corroded surface, the immersed samples in seawater were investigated by SEM after rinsing with deionized water and drying with nitrogen.

3. Analysis results

3.1. Microstructure analysis

Fig. 1 reveals that the $Al_2Cr_5Cu_5Fe_{53}Ni_{35}$ is a single-phase FCC solid solution material. The peaks are exclusive response of the disordered FCC phase, similar to the FeNi intermetallic compound, which can be indicated by the (1 1 1) and (2 0 0) super-lattice peaks, followed by the (2 2 0), (3 1 1) and (2 2 2) peaks. The PDF card number for the Tetrataenite phase used in the XRD analysis corresponds to the following code: 01–71–8321.

The EBSD patterns were indexed using the FCC iron phase, and the maps presented in Fig. 2 show that the $Al_2Cr_5Cu_5Fe_{53}Ni_{35}$ alloy contains only a single FCC phase. However, the grain size of the alloy is quite large with an average grain size of 500 μm. The EDS maps, as depicted in Fig. 3, depict that each element is homogeneously distributed in the matrix space and the chemical composition closely matches with data provided in Table 1. The electron-backscattered diffraction (EBSD) and the energy-dispersive spectrometer (EDS) both indicate that the $Al_2Cr_5Cu_5Fe_{53}Ni_{35}$ alloy can be deemed as a long-range order, single-phase, FCC crystal structure, which is consistent with previous XRD outcomes.

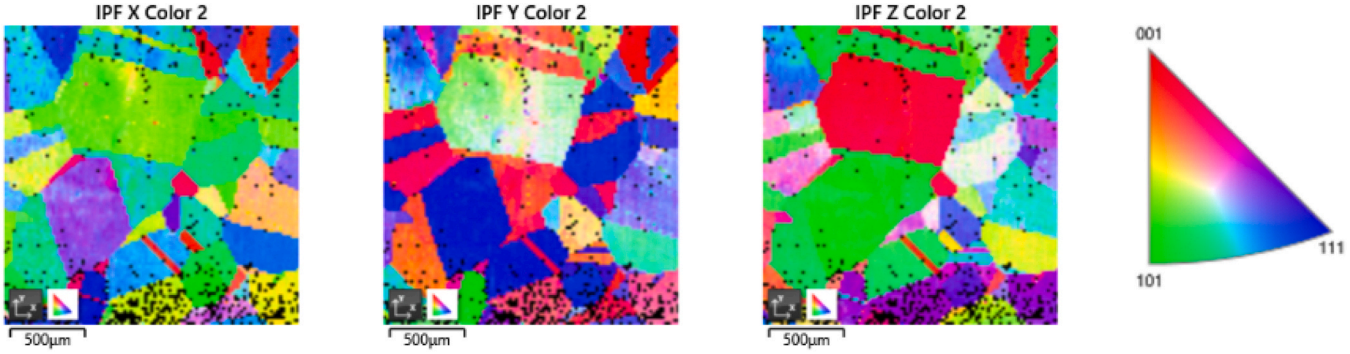

Fig. 2. Electron-backscattered diffraction (EBSD) mapping of the microstructure of $Al_2Cr_5Cu_5Fe_{53}Ni_{35}$ alloys along different axis.

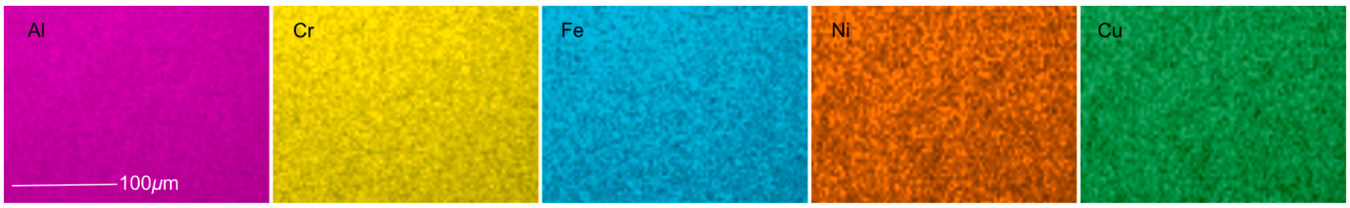

Fig. 3. Energy-dispersive X-ray spectroscopy (EDS) mapping shows the elemental distribution in $Al_2Cr_5Cu_5Fe_{53}Ni_{35}$ alloys.

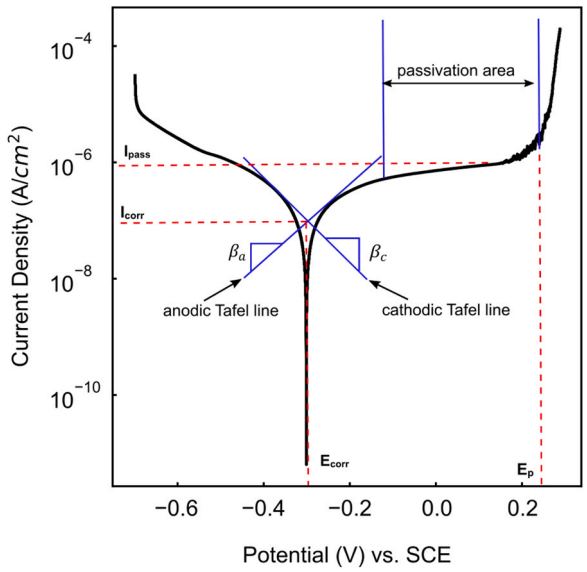

Fig. 4. Typical potentiodynamic-polarization curve for the explanation of the electrochemical parameters.

3.2. Potentiodynamic and potentiostatic measurements

To study the limit of the passive stability of the current material, the potentiodynamic-polarization method is employed [36]. Several electrochemical parameters are used to characterize the corrosion properties of the material as indicated in Fig. 4. The E_{corr} stands for the corrosion potential in the open circuit situation, I_{corr} is the corrosion current density, which is determined from the Tafel plot by extrapolating the linear portion of the polarization curve near E_{corr}. Meanwhile, the β_a and β_c are the anodic and cathodic Tafel slopes, respectively; and the E_p represents the critical pitting potential and I_{pass} is the current density in the passivation area.

Fig. 5 shows the corresponding potentiodynamic results obtained at different temperatures and scan rates in seawater electrolyte. The resulting electrochemical parameters as a function of electrolyte temperature and scan rate are displayed in Table 3. From the plots, it can be inferred, especially for $0.1 mVs^{-1}$ that as temperature increases, the E_p decreases whereas the I_{pass} increases. This indicates that the resistance to localized corrosion diminishing accordingly. Moreover, the potential difference between the OCP and the pitting potential decreases with increasing temperature, which could be attributed to the weakening and further instability of the passive film that may lead to its breakdown. Likewise, the I_{corr} slightly increases along with the rising temperature, which means that the rate at which the corrosion takes place as a function of the temperature is fairly invariant, especially for levels below 50 °C. In Figs. 5(c) and (d), an obvious transition from a steady-state passivity at 25°C to an active corrosion state at 50°C was observed, which specifies that the stability of passive film decreases significantly at a certain temperature between 25°C and 50°C. As per the influence of the scan rate on the passivity response of the metal surface, certainly a significant susceptibility of the passive film can be observed as I_{corr} and I_{pass} surge as a function of the scan rate and temperature with larger passivation areas, mainly for temperatures below 25 °C. Similar tendency, but with lesser activation of the oxide film is observed for greater temperatures, where the lower scan rate ($0.1 mVs^{-1}$) exhibits some metastable pitting behavior in the passive region (defined as the occurrence of a current fluctuation/serration during polarisation as depicted by the solid black line).

To further study the stability of the oxide film, a set of potentiostatic experiments were conducted to obtain additional information regardless the dynamic effects commonly induced by the polarization scan rate [37]. The behavior of the current transients in seawater near the OCP conditions (OCP + 50 mV) at different temperatures are shown in Fig. 6. As it can be seen the metastable pitting activity increases with the solution temperature (current intensity oscillation), especially for temperatures of 60 °C and 75 °C, whereas the steady-state oxide film protects firmly the metal surface for lower temperatures. This analysis provides additional support to the previous dynamic based potential polarisation results, where the pitting potential strongly depends on temperature. However, the occurrence of metastable pitting is somehow related to the magnitude of the scan rate as the current density perturbations are more apparent in lower sweeping rate than higher ones as they tend to disappear accordingly.

On the other hand, the Tafel plots for the material tested in different seawater solutions with varying chloride concentrations and temperatures at fix scan rate of 0.1 mV/s are presented in Fig. 7. The chloride concentrations of the solutions considered in this study are 0.55 mol/L for seawater, 0.055 mol/L for 0.1 x diluted seawater, and 5.5 mol/L for 10 x condensed seawater. Figure 7 displays that the pitting potential diminishes with increasing chloride concentration in all temperature intervals, as is normally observed in iron-based alloys [38]. Also, the current density within the passive range increases suggesting that the corrosion rate would eventually escalates since there are more chloride ions in the solution. And it is obvious that the potential difference between the OCP and the pitting potential drops as chloride concentration climbs, indicating that the stability of the passive film decreases with higher [Cl^-].

Likewise, dynamic effects on passive film formation were also removed by performing potentiostatic analysis on samples immersed in simulated seawater solutions at different concentrations. Fig. 8 illustrates the the effect of the chloride concentration on typical chronoamperometry transients obtained at near OCP conditions, as observed from the experiments performed at 25°C (Fig. 8(a)) and 50°C (Fig. 8(b)). The lack of oscillation in the current transients presented in Fig. 8(a) can be attributed to the absence of corrosion activity in the form of pitting as the electromotive force necessary for this process has not been achieved and thus the protecting oxide film remains unaltered regardless solution concentration. However, as depicted in Fig. 8(b), when the temperature is 50 °C, the weakness of the passivation on the alloy surface is related to the chloride concentration. Higher chloride concentration will lead to the activation of metastable pittings. That is, there is a steep climb of the current after a few seconds of starting the experiment in the 10 x seawater solution suggesting controlled-diffusion of electroactive

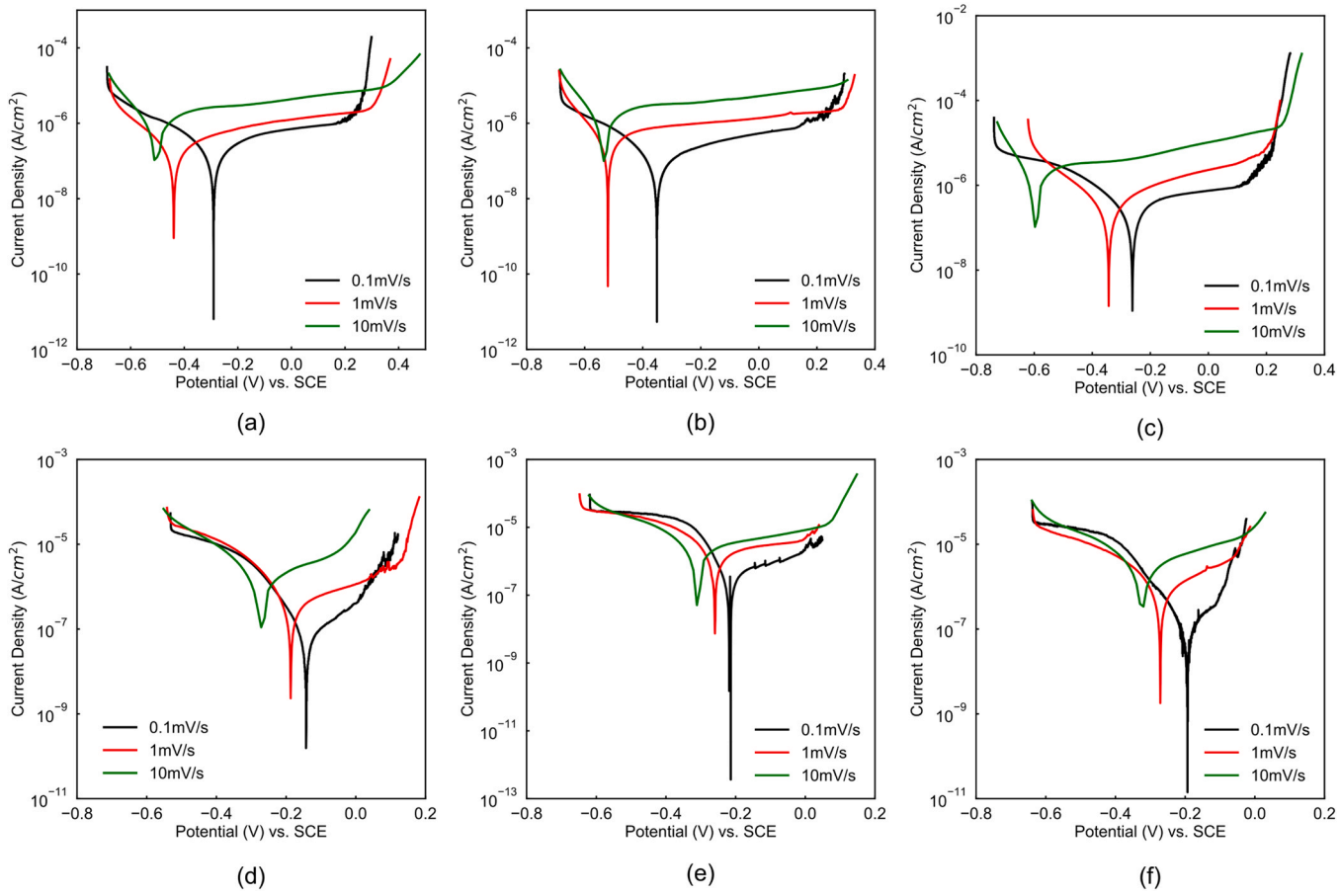

Fig. 5. Potentiodynamic-polarization curves of $Al_2Cr_5Cu_5Fe_{53}Ni_{35}$ alloys at (a) 2°C, (b) 10°C, (c) 25°C, (d) 50°C, (e) 60°C, (f) 75°C with various scan rates ranging from 0.1 mV/s to 10 mV/s in seawater.

Table 3
Electrochemical parameters of $Al_2Cr_5Cu_5Fe_{53}Ni_{35}$ alloys in the seawater with scan rates of 0.1 mV/s, (1 mV/s), and [10 mV/s] at different temperatures.

Temperature	E_{corr} (mV vs. SCE)	I_{corr} (μA/cm^2)	β_a (mV/dec)	β_c (mV/dec)	E_p (mV vs. SCE)	ΔE (mV vs. SCE)	I_{pass} (μA/cm^2)
2°C	− 248.09	0.024	80.7	− 57.5	357.05	605.14	0.470
	(− 443.31)	(0.133)	(142.6)	(− 95.1)	(347.75)	(791.06)	(1.273)
	[− 515.25]	[0.252]	[88.2]	[− 55.6]	[461.75]	[977.00]	[4.533]
10°C	− 357.10	0.018	76.1	− 39.9	305.90	603.01	0.468
	(− 526.60)	(0.179)	(180.3)	(− 81.8)	(311.66)	(838.26)	(1.286)
	[− 552.70]	[0.491]	[120.4]	[− 77.6]	[352.6]	[905.3]	[4.917]
25°C	− 258.11	0.022	26.4	− 33.9	275.42	533.53	0.605
	(− 348.70)	(0.201)	(159.5)	(− 91.6)	(232.02)	(580.72)	(2.083)
	[− 600.88]	[0.837]	[157.1]	[− 81.1]	[289.72]	[890.6]	[6.050]
50°C	− 144.76	0.023	64.3	− 35.5	143.35	288.11	0.669
	(− 207.80)	(0.210)	(167.6)	(− 73.1)	(153.25)	(361.05)	(2.350)
	[− 308.19]	[0.438]	[143.3]	[− 88.6]	[11.25]	[319.44]	[5.104]
60°C	− 200.31	0.034	20.5	− 15.2	87.49	277.80	0.793
	(− 261.34)	(0.549)	(108.8)	(− 56.2)	(48.06)	(309.40)	(3.145)
	[− 319.01]	[0.716]	[95.3]	[− 74.6]	[81.06]	[400.07]	[5.420]
75°C	− 196.34	0.028	40.8	− 31.9	28.08	224.42	0.885
	(− 279.65)	(0.432)	(163.5)	(− 68.0)	(− 3.22)	(276.43)	(2.833)
	[− 335.62]	[1.154]	[126.9]	[− 97.2]	[14.78]	[350.4]	[6.793]

species, which is consistent with the potentiodynamic results shown in Fig. 7(d). However, uniform passive film formation is steadily built-up in 0.1 x seawater, which agrees with the flat chronoamperometry transient in Fig Fig 8(b).

3.3. EIS results

The electrochemical impedance spectroscopy is a steady state method of characterizing many of the electrical properties of materials and their interfaces with the electronically conducting electrodes [39]. Fig. 9(a) and (b) display the Nyquist and Bode plots of the studied alloy, under different temperatures in the seawater solution. The Nyquist plots are semicircle arcs with centers below the x-axis. As the temperature increases, the diameter of the depressed semi-circle decreases, indicating a potential detrimental influence of the passive film. The phase plots at lower temperatures specify the characteristics of capacitor-like behavior resulting in a time constant, showing a slightly constant mid-to-low frequency

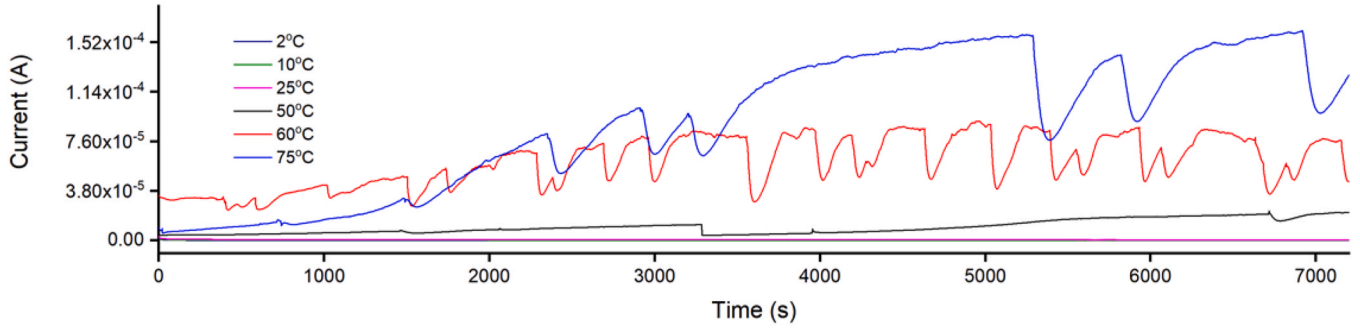

Fig. 6. Effect of temperature on the chronoamperometry transients obtained at the recorded OCP + 50 mV for $Al_2Cr_5Cu_5Fe_{53}Ni_{35}$ alloys in seawater.

phase-angle magnitude close to 60 degrees. When temperature rises to 25°C, the low frequency phase angle lessens revealing the capacitive-like behavior decreases. Moreover, for the range 50°C - 75°C, the surface heterogeneity, especially caused by the erosion, the one-time constant could in reality be the overlapping of two-time constants [40,41]. The lower temperature cases can be associated with the passive film formed on the alloy surface. However for the cases with a temperature higher than 25°C, the second-time constant relates to the electrolyte/alloy interface via defects resolved. These latter case suggests that the chloride initiates the breakdown process of the passive film [42,43]. It can be demonstrated from the varied shapes of the Bode plots that the passive films become more vulnerable with increasing temperature, especially at the temperatures above 25°C. This transition from stable passivity to film breakdown is in agreement with previous results obtained with the polarization analysis shown in Fig. 5: at higher temperatures (above 25°C), the $Al_2Cr_5Cu_5Fe_{53}Ni_{35}$ alloys change from the Tafel region into the active corrosion region, while at lower temperatures, the alloys change directly from the Tafel region towards the stable passive region, without showing an active to passive transition. The EIS analysis indicates that the $Al_2Cr_5Cu_5Fe_{53}Ni_{35}$ alloy could spontaneously form the protective film at a lower temperatures to prevent further

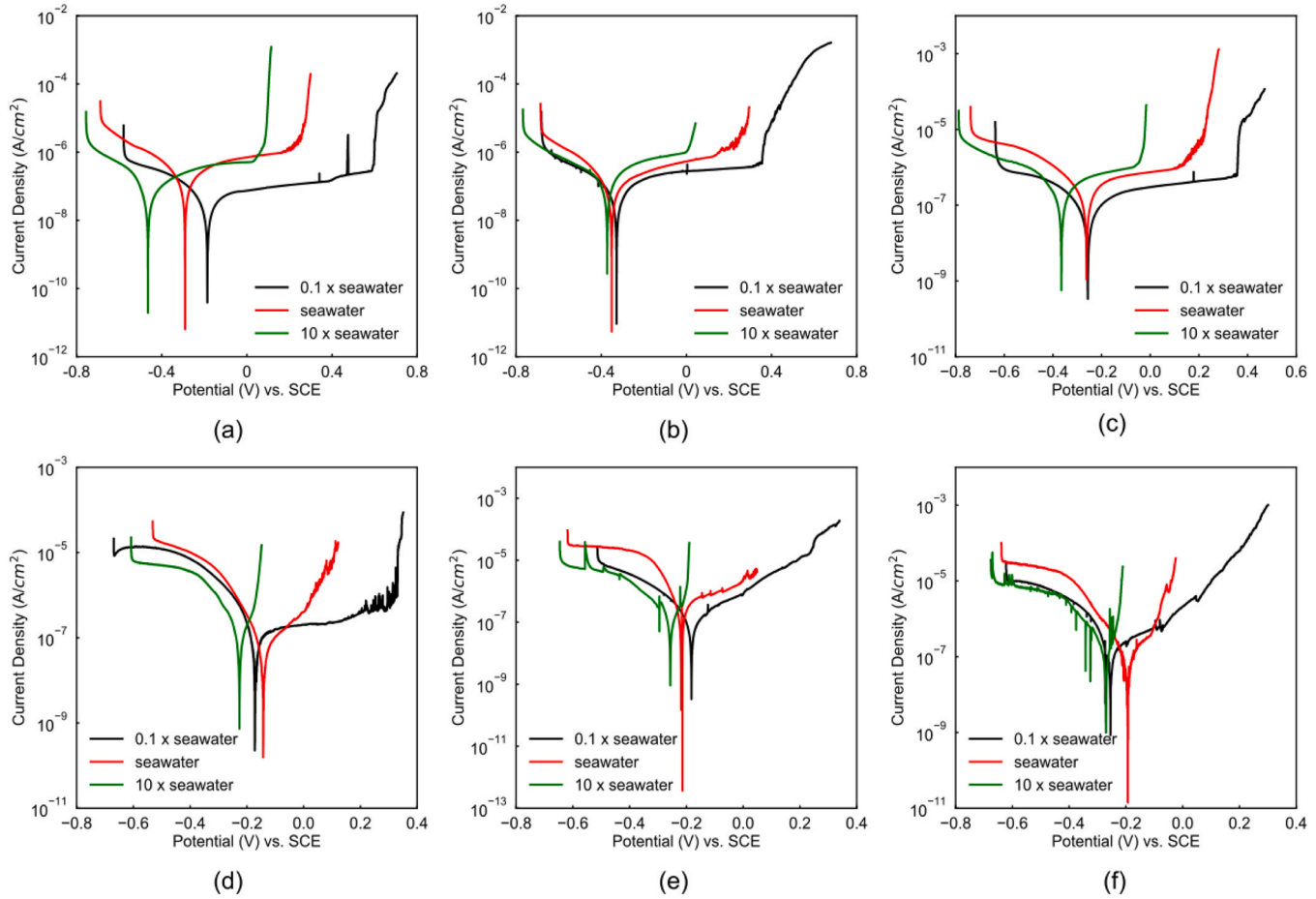

Fig. 7. Potentiodynamic-polarization curves of $Al_2Cr_5Cu_5Fe_{53}Ni_{35}$ alloy at (a) 2°C, (b) 10°C, (c) 25°C, (d) 50°C, (e) 60°C, (f) 75°C in various chloride concentration solutions with a scan rate of 0.1 mV/s.

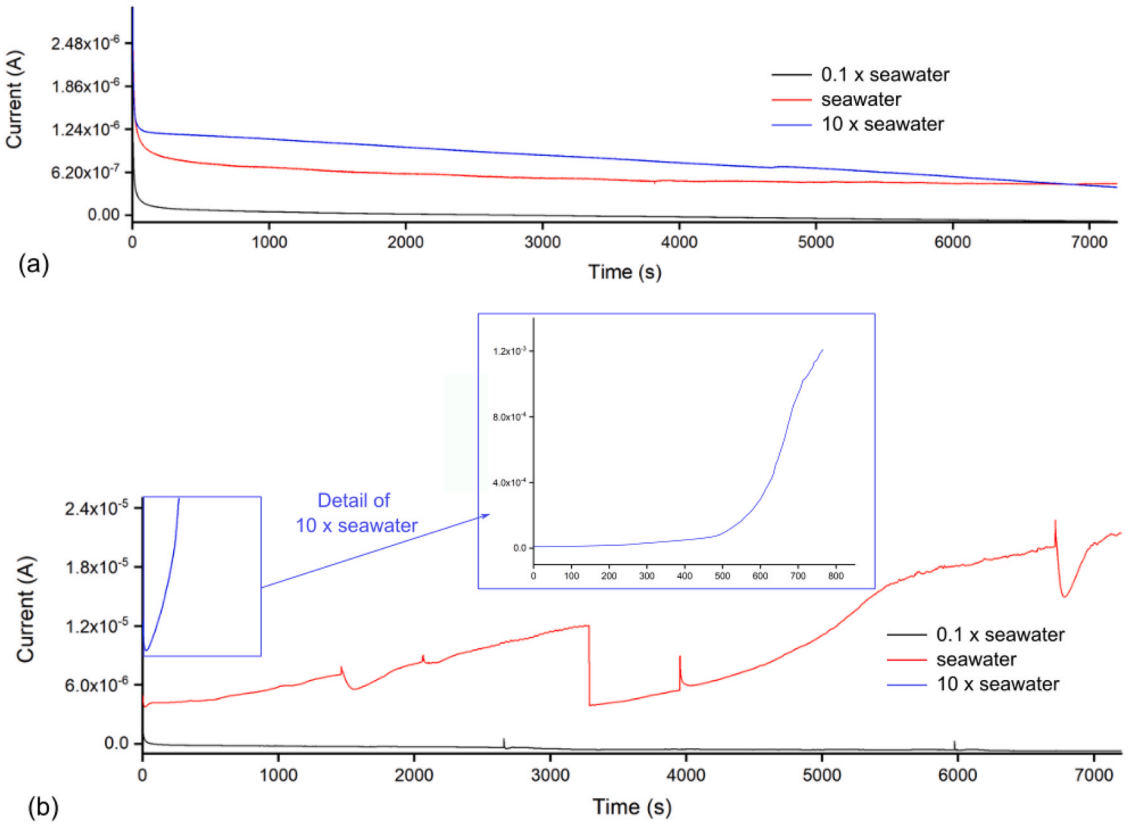

Fig. 8. Effect of chloride concentration on the chronoamperometry transients obtained at the recorded OCP + 50 mV for $Al_2Cr_5Cu_5Fe_{53}Ni_{35}$ alloys. (a) at 25°C, (b) at 50°C.

dissolution, however when the temperature increases higher than 50°C, the protective film is hardly form on the surface leading the material to actively corrode.

Figure 9(c) displays the equivalent electrical circuit designed to fit the experimental results at 2°C, 10°C and 25°C, while Fig. 9(d) shows the equivalent electrical circuit for the three selected temperature levels of 50°C, 60°C and 75°C. As shown in Fig. 9(c), the surface is covered with a protective passive layer, which is consistent with the polarization-dynamic results previously discussed in above subsection. This equivalent circuit is simply composed of the resistance of the electrolyte ($R_{electrolyte}$), charge-transfer resistance (R_{pass}), and a constant phase element (CPE_{pass}) used to characterize the pseudo-capacitance properties of the passive layer [44]. Moreover, the equivalent circuit designed for the three higher temperature levels is composed of two parts: the first circuit describes the passive film formation (similar to the equivalent circuit of lower temperatures cases); whereas the second one is a series-connected circuit to the R_{pass} used to describe the corrosion process which occurs in the sensitive area where local attack (pits) are likely to form due to the surface defects [45]. The active mechanism of film breakdown can be characterized as an equivalent circuit having a charge-transfer resistance (R_{ct}) and a pseudo-double-layer capacitance (CPE_{dl}) covering the pit surface partially. The impedance [46] of the CPE is described by the expression

$$Z_{CPE} = Y_0^{-1}(i\omega)^{-\alpha} \tag{1}$$

where Z_{CPE} is the impedance of the CPE, Y_0 is the proportionality factor, i is the imaginary unit, ω is the angular frequency, and α is the phase shift [47]. The effective capacitance [46] associated with the CPE can be expressed by the formula proposed by Hsu and Mansfeld for studies on passive film [48,49].

$$C_{eff} = Y_0^{1/\alpha} R_f^{(1-\alpha)/\alpha} \tag{2}$$

The Nyquist and Bode curves of the $Al_2Cr_5Cu_5Fe_{53}Ni_{35}$ alloy are included in Fig. 9(a) and (b). The fitted lines are in good agreement with the experimental results indicating the suitability of the proposed models to describe the electrical characteristics of the passive film of the alloy in the solution. The theoretical-simulated impedance parameters are summarized in Table 4. As it can be seen, the charge-transfer resistance decreases with the increasing of temperature for both passive film and active dissolution due to passivity breakdown or activation surface, which illustrates the influence of the temperature on the corrosion resistance. The Y_0 coefficient in the CPE_{pass} decreases, while the Y_0 in the CPE_{dl} increases with increasing temperature, which indicates that when the temperature exceeds 50°C, the porosity in the film plays a significant role on the corrosion resistance of passive film. The α value, though, is found to have a negative effect with respect to the temperature. According to Hirschorn and Orazem [46] the passive film thickness (d_{eff}) of the $Al_2Cr_5Cu_5Fe_{53}Ni_{35}$ can be calculated based on the data obtained from EIS by means of

$$d_{eff} = \frac{\varepsilon\varepsilon_0}{C_{eff}} \tag{3}$$

where ε is the relative dielectric constant taken as 12, which is suitable for HEAs [50], while ε_0 is the permittivity of vacuum whose value is 8.8542×10^{-14} F/cm. In Table 4 the estimate film thicknesses for each considered temperature are provided.

From the EIS study, $Al_2Cr_5Cu_5Fe_{53}Ni_{35}$ has better corrosion resistance at lower temperatures than higher ones. Evidence indicates that the equivalent electric circuit to describe the properties of the interface translates from a simple passive film to a passive film with a number of active areas, which is agreed upon with the potentiodynamic-polarization analysis for higher temperature levels. On the other hand, oxide film thickness estimation based on effective capacitance does not exhibit an overall temperature dependence, but it does when is considered as a function of the chosen equivalent

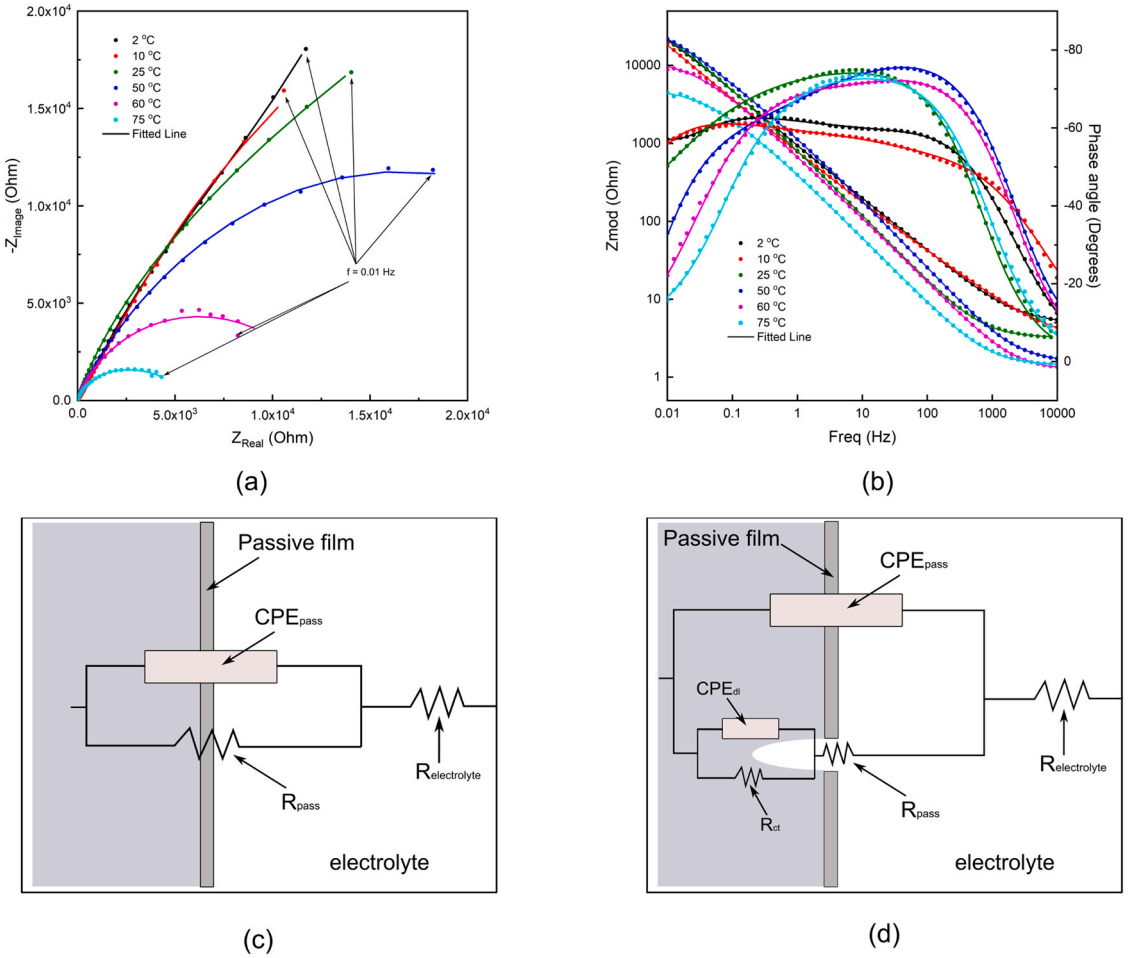

Fig. 9. The effect of temperature on the (a) Nyquist and (b) Bode plots of $Al_2Cr_5Cu_5Fe_{53}Ni_{35}$ alloys measured at open circuit potential with a sinusoidal potential amplitude of 10 mV, running from 10 kHz to 10 mHz in seawater. The equivalent electrical circuit representative of the electrode interface for the alloys at (c) 2°C, 10°C, 25°C and (d) 50°C, 60°C, 75°C.

circuit illustrated in Fig. 9c and d. For instance, C_{eff} varies slightly in the temperature range of 2°C ≤ T ≤ 25°C, while certain improvement of potential corrosion E_p is observed (see Fig. 5(a), (b) and (c)). Hence, the film thickness oscillates accordingly with an average value of 8.0 nm. This response is consistent with the equivalent circuit model defined in Fig. 9(c) that represents a homogeneous time-constant distribution. Conversely, the model in Fig. 9(d) for T ≥ 50°C yields an increase of oxide film thickness with respect to temperature, which is consistent with Eq. 3 that indicates an inverse relationship between film thickness and effective capacitance with a compositional configuration of the passive layer [21,46].

3.4. XPS analysis

The protective oxide films formed on the surface of materials have a direct effect on the dissolution process . In order to obtain more information about the passive film products, XPS is usually utilized to study the chemical compositions of oxide films [51]. The Fe $2p_{3/2}$, Ni $2p_{3/2}$, Cr $2p_{3/2}$, Al 2p, Cu $2p_{3/2}$, and O 1 s spectra of the $Al_2Cr_5Cu_5Fe_{53}Ni_{35}$ alloy are presented in Fig. 10. The Al 2p spectra contain the metallic-state aluminum, aluminum oxide, and hydroxide [52]. Similarly, the Ni $2p_{3/2}$, Cr $2p_{3/2}$ spectra contain the metallic-state metal, the oxide, and the hydroxide product, while the Fe $2p_{3/2}$ spectra contain the metallic-state metal, and the oxide with different valence [53]. The Cu $2p_{3/2}$ spectra contain metallic-state Cu, and oxide product only, without hydroxide product [54]. The O 1 s spectra are composed of the O^{2-} and OH^- peaks. From the fitting results presented in Fig. 10, the spectra were fitted well with the metallic state or the oxide of each element. The cumulative fit peaks agree well with the raw data. According to the area under the peaks, the percentage atomic concentration of each element [20] can be computed by

Table 4
Equivalent circuit element values for EIS data of $Al_2Cr_5Cu_5Fe_{53}Ni_{35}$ alloys in seawater.

Temp.	R_{pass}	R_{ct}	$R_{electrolyte}$	CPE_{pass} parameters		CPE_{dl} parameters		C_{eff}	d_{eff}
	(Ωcm^2)	(Ωcm^2)	($\Omega\,cm^2$)	Y_0 ($Fcm^{-2}s^{n-1}$)	α	Y_0 ($Fcm^{-2}s^{n-1}$)	α	(Fcm^{-2})	(nm)
2°C	1.54×10^7	N/A	61.8	4.23×10^{-5}	0.71	N/A	N/A	1.18×10^{-4}	9.0
10°C	1.58×10^7	N/A	68.4	6.08×10^{-5}	0.66	N/A	N/A	1.74×10^{-4}	6.1
25°C	3.38×10^6	N/A	52.2	5.90×10^{-5}	0.85	N/A	N/A	1.19×10^{-4}	8.9
50°C	2.00×10^6	1.48×10^6	38.4	2.43×10^{-5}	0.87	2.67×10^{-6}	0.78	3.77×10^{-5}	28.2
60°C	1.87×10^6	1.26×10^6	28.8	1.40×10^{-5}	0.85	8.57×10^{-5}	0.82	2.00×10^{-5}	53.1
75°C	9.87×10^5	7.14×10^5	24.6	7.88×10^{-6}	0.85	8.50×10^{-5}	0.86	9.24×10^{-6}	115.1

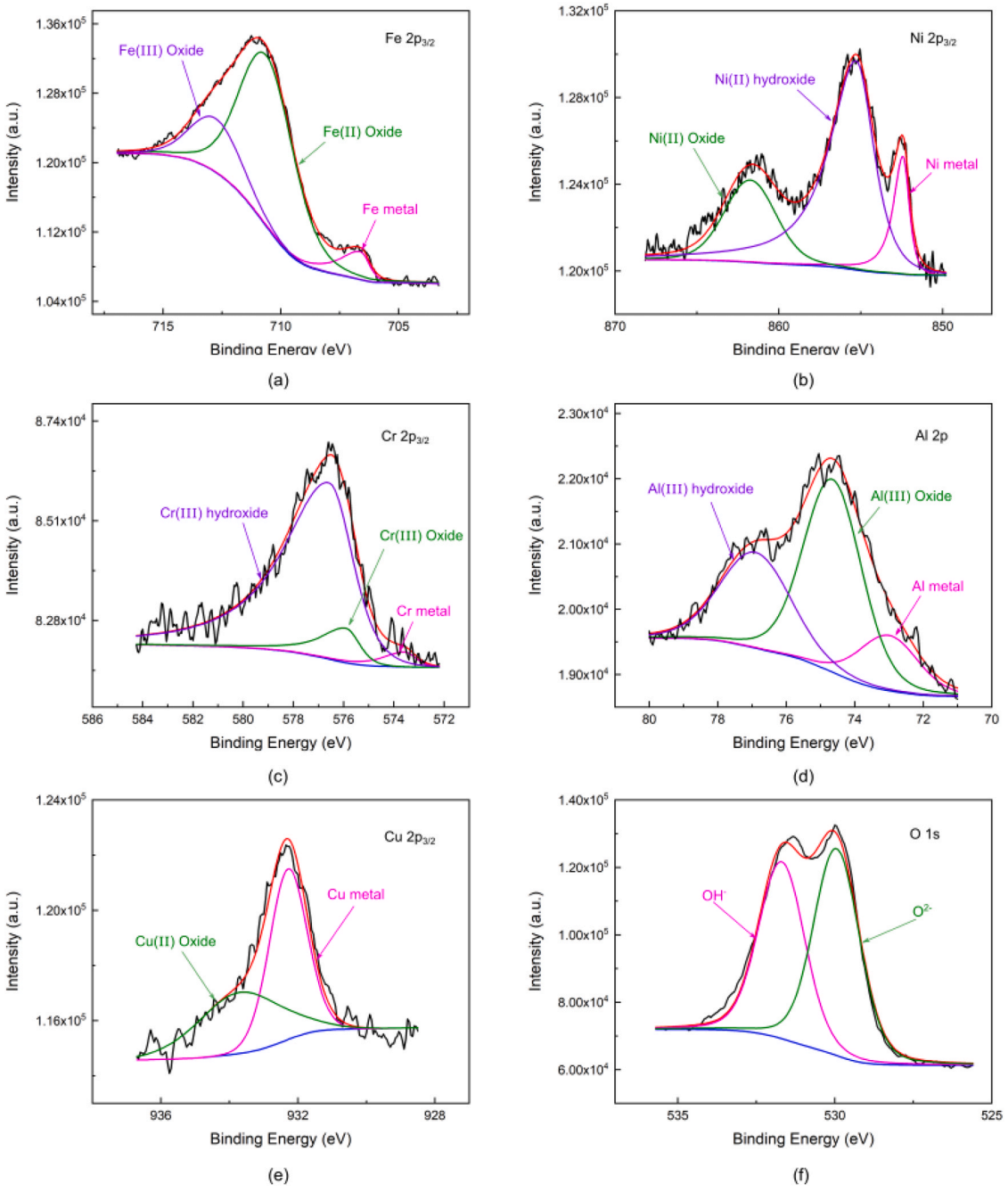

Fig. 10. (a) Fe $2p_{3/2}$ (b) Ni $2p_{3/2}$ (c) Cr $2p_{3/2}$ (d) Al 2p (e) Cu $2p_{3/2}$, and (f) O 1 s spectra of $Al_2Cr_5Cu_5Fe_{53}Ni_{35}$ alloys after immersed in seawater for 24 h at room temperature.

$$X_i = 100\frac{A_i}{\sum_{i=1}^{n} A_i} \tag{4}$$

where X_i stands for the atomic percent of the ith element, n is the total number of elements in the material, which is 5 in this case, and A_i is the adjusted intensity [20], which is given by

$$A_i = \frac{J_i}{R_i K} \tag{5}$$

where J_i is the measured intensity, R_i is the relative sensitivity factor which can be obtained from CasaXPS software, and K is the kinetic energy. The calculation results of the chemical compositions for the passive film are presented in Table 5.

Based on the information given by Table 5 and Fig. 10, the XPS results indicate that the dissolution rate of each element has significant differences. It can be observed that the Al is mostly present in the alloy's passive film products formed at room temperature. The Al_2O_3 is commonly used as coating material due to its insulated behavior as reported in the literature [55,56]. Hence, the large amount of Al_2O_3 in the passive film serves as a protective layer at the outer surface of the material to prevent further corrosion. It is consistent with the stable passive behavior observed in the 25°C potentiodynamic-polarization curves as well as the lack of

Table 5
Chemical compositions (at%) of passive film formed on the surface of $Al_2Cr_5Cu_5Fe_{53}Ni_{35}$ alloys after immersed in seawater for 24 h at room temperature.

Element	Al	Cr	Cu	Fe	Ni	O
at%	21.2	1.3	0.7	4.8	2.7	69.3

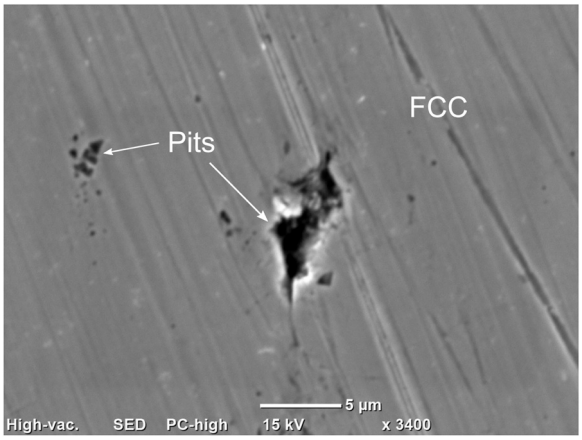

Fig. 11. SEM micrograph for $Al_2Cr_5Cu_5Fe_{53}Ni_{35}$ alloys after immersed in seawater for 21 days at room temperature.

metastable pitting activity depicted by the 25°C current transient in potentiostatic experiment.

3.5. Photomicrograph of corroded surface

Fig. 11 illustrates the surface morphology of the $Al_2Cr_5Cu_5Fe_{53}Ni_{35}$ alloy after immersion in simulated seawater solution for 21 days at room temperature. It can be seen that tiny pits are sparsely formed in the FCC phase, while the remnant area remains smooth, which contributes to the stable passivation process. As indicated by the polarization tests at room temperature, the protective films are formed spontaneously at the OCP to prevent the metallic alloy from active corrosion. Moreover, the lack of the oscillation in the current transient presented in Fig. 8(a) reveals that few metastable pittings develop at room temperature due to the occurance of discontinuity-like porous on the passive film.

4. Discussion

4.1. Point Defect Model (PDM) analysis

Over the past 40 years, there have been many studies related to measuring the pitting potential. Several theories have been developed to explain the passivity breakdown and pit nucleation, but only the Point Defect Model (PDM) has achieved certain success to characterize the linear dependence of the pitting potential on the log [Cl^-] with a slope greater than $2.303RT/F$, and the pitting potential relation with the potentiodynamic-polarization scan rate [57].

The point Defect Model states that the cation vacancies which are generated at the interface between the film and the solution will move to the interface of the film and the metal, and this movement can be annihilated by cation injection into the film from the metal following the Schottky-pair type reaction as expressed by the following equations [57]

$$m + V_M^{\chi'} \rightarrow M_M + v_m + \chi e' \tag{6}$$

$$m \rightarrow M_M + \frac{\chi}{2}V_O^{\cdot\cdot} + \chi e' \tag{7}$$

where m and v_m are metal atom and metal vacancy in the metal phase, while $V_M^{\chi'}$ and M_M are cation vacancy and metal cation in cation site . Noting that the above equations set represent the fundamental reactions that occur in the metal/film interface only, and include the nonconsevative process involving film generation given by the two first terms of the oxidation reaction in Eq. (7). The cation vacancies condense at the metal/film interface whether the annihilation rate of cation vacancies (J_m) is smaller than the enhanced flux of cation vacancies (J_{ca}). Furthermore, when the areal concentration in the condensate exceeds a critical value (ξ), the local separation of the barrier layer from the substrate metal will occur, which will continue at the edge of blister leading the expansion of an already formed blister while it dissolves at the blister/solution interface. Further details are not given here for the sake of the space, but interested readers are refered to ref. [57].

The picture PDM draws is that the cation vacancy condenses when the enhanced flux of the cation vacancies exceeds a critical value first, vacancy condensation then causes this region to expand and form high local discontinuous areas and these "weak points" on the surface are where passivity breakdown occurs [30–32,58].

The PDM asserts that the pitting potential for a single site on the passive film can be determined by

$$E_p = \frac{4.606RT}{\chi\alpha F}\log\left(\frac{b}{D}\right) - \frac{2.303RT}{\alpha F}\log[Cl^-] \tag{8}$$

$$b = \frac{RTJ_m\,\Omega}{F\chi\varepsilon N_v} \times \exp\left(\frac{\Delta G_s^0 + \frac{\chi}{2}\Delta G_A^0 - \frac{\chi}{2}\beta F\mathrm{pH} - \frac{\chi}{2}F\phi_{f/s}^0}{RT}\right) \tag{9}$$

where T represents the temperature; χ is the oxide stoichiometry; α and β are the dependencies of potential drop across the film/solution interface ($\phi_{f/s}$) on the applied potential and pH, respectively, $\phi_{f/s}^0$ is the value of $\phi_{f/s}$ in the standard state of $E = 0$ and pH = 0; D stands for the cation vacancy diffusion coefficient; the Ω is defined as the volume per mole of the cation in the barrier film and the ε is the electric field strength. The energy term $\Delta G_s^0 + \frac{\chi}{2}\Delta G_A^0 - \frac{\chi}{2}F\phi_{f/s}^0$ is used to describe the energy related to the absorption of aggressive anions into $V_O^{\cdot\cdot}$ [59]. And the others are standard chemistry constants such as R is the gas constant, F is Faraday's constant, and N_v is Avogadro's number. According to the PDM theoretical framework, the relative stability of the passive layer is largely dependent on the behavior of the polarizability of the film/solution interface, α, and the rate of annihilation of the cation vacancies at the metal/film interface, J_m [60].

As indicated in Eq. 8, the pitting potential is linear regarding the chloride concentration, and the slope steepness is associated to the degree of polarizability of the film/solution interface (α). From the relationship between E_p and [Cl^-] described in Eq. 8, the intercept at low [Cl^-] can be used to compute the b/D ratio, which describes how fast the metal cations are used at the metal/film interface. It can be used as an indicator of the stability of the passive film. Figure 12(a) shows the effect of [Cl^-] on the pitting potential, since the pitting potential here is obtained by potentiostatic staircase method, there is no scan rate influence on it. The results presented in 12(a) are consistent with the prediction of PDM, as the pitting potential (E_p) of $Al_2Cr_5Cu_5Fe_{53}Ni_{35}$ decreases linearly with the increasing of the logarithmic chloride concentration (log[Cl^-]), and the slope changes with the polarizability of the film/solution interface. The slope decreases, so that the α value will become larger when the temperature increases.

According to Eq. 9, the rate of cation annihilation at the metal/film interface, J_m needs to be evaluated experimentally with the effect of the scan rate included in the potentiodynamic-polarization experiments. On the basis of PDM description, the pitting potential exhibits a linear dependency with the square root of the scan rate ($v^{1/2}$) as indicated by Eq. 10 [37]

$$E_p(v) = \left(\frac{2\xi RT}{J_m\chi\alpha}\right)^{1/2} v^{1/2} + E_p(v=0) \tag{10}$$

where ξ is the critical areal cation vacancy concentration, which is related to the crystal structure of the metal oxide and the corresponding metal substrate [30]. The parameters value used in Point Defect Model are summerized in Table 6 and 7.

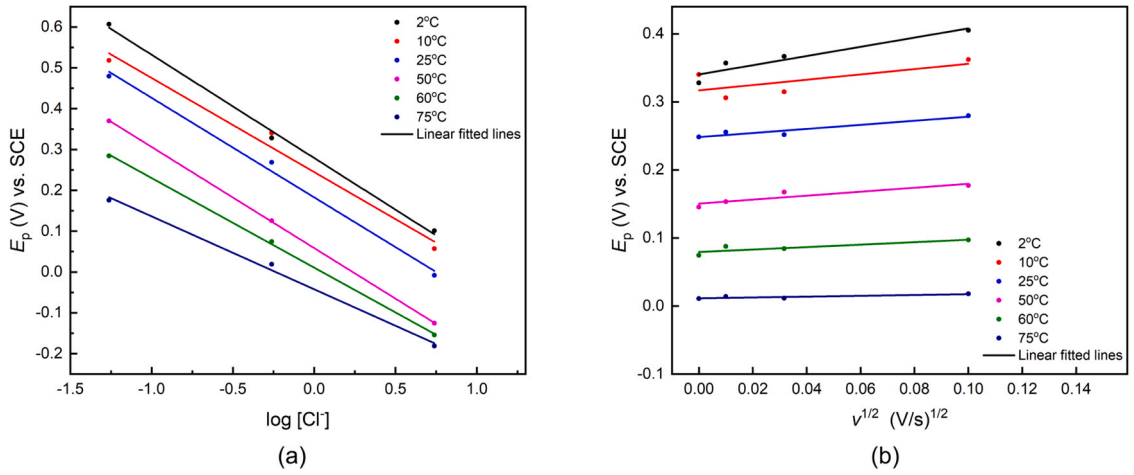

Fig. 12. Effect of temperature in the relationship between the (a) pitting potentials vs. chloride concentration, and (b) pitting potentials vs. potentiodynamic scan rate of $Al_2Cr_5Cu_5Fe_{53}Ni_{35}$ alloys.

Table 6
The slope and intercept of the fitted results about the linear relationship ($y = Ax + B$) between E_p vs. log[Cl^-] shown in Fig. 12(a) and E_p vs. $v^{1/2}$ shown in Fig. 12(b).

Temperature (°C)	E_p vs. log[Cl^-]			E_p vs. $v^{1/2}$		
	A	*B*	R^2	*A*	*B*	R^2
2	−0.253	0.2792	0.99644	0.676	0.3403	0.90691
10	−0.2305	0.2448	0.98288	0.390	0.3169	0.47880
25	−0.2438	0.1829	0.99397	0.300	0.2482	0.90723
50	−0.2477	0.0587	0.99995	0.291	0.1505	0.85449
60	−0.2195	0.0108	0.99940	0.180	0.0794	0.74927
75	−0.1787	−0.0423	0.99515	0.059	0.0114	0.72412

Table 7
Parameter values used in the PDM calculating for $Al_2Cr_5Cu_5Fe_{53}Ni_{35}$ alloy in seawater solution (pH = 8.1 ± 0.1) with different temperature.

Parameter	Value	Units	Source
F, Faraday's constant	96487	C/equiv	Fundamental constant
R, gas constant	8.3144	J/(mol K)	Fundamental constant
N_v, Avogadro's number	6.023×10^{23}	no./mol	Fundamental constant
χ, the barrier layer stoichiometry (Fe_2O_3)	3	–	Assigned[31]
Ω, molar volume of Fe_2O_3 per cation	15.27	cm^3/mol	Assigned[31]
ε, the electric field strength	5×10^6	V/cm	Assigned[30]
ξ, the critical areal cation vacancy concentration	3.3×10^{14}	no. $/cm^2$	FromFig. 12(b)
$w = \Delta G_s^0 + \frac{\chi}{2}\Delta G_A^0 - \frac{\chi}{2}F\phi_{f/s}^0$	-23.4	kJ/mol	FromFig. 12(a)
β, the dependence of $\phi_{f/s}$ on pH	-0.01	V	Assigned[30]

The E_p vs. scan rate outcomes obtained from potentiodynamic-polarization experiments are depicted in Fig. 12(b). As it can be observed, under the potentiodynamic-polarization conditions, the pitting potential is found to be linearly dependent with respect to the square root of the scan rate. That is, the higher the scan rate is, the larger the pitting potential. The results shown in Fig. 12(b) are consistent with the PDM description in Eq. 10 [37,61]. It can be inferred from the decreasing slope magnitude shown in Fig. 12(b) indicates that the value of J_m increases with the solution temperature as well. This is consistent with the surging of the apparent passive current density observed in experiments as shown in Fig. 5 and Fig. 6.

The influence of the solution temperature on the polarizability of the precipitated outer layer (α) and the rate of annihilation of the cation vacancies at the metal/film interface (J_m) is presented in Fig. 13. The values of α and J_m were obtained from the PDM relationships shown in Eq. 8 and 9, with the linear fitting analysis of the data presented in Fig. 12(a) and 12(b). It can be seen, both α and J_m values increase with temperature. According to the passivity description of PDM [62], these results indicate that the rise of temperature is responsible for undermining the passive film formed on the surface of $Al_2Cr_5Cu_5Fe_{53}Ni_{35}$ alloy. Moreover, the upper limit of the J_m value is 2×10^{17} within the barrier layer of Cr_2O_3 [63], which is typically lower than the J_m of the current alloys revealing that the passive film is constituted by additional other elements rather than Cr solely. This can be proved by the chemical compositions of the passive film shown in the XPS results, the smallest amount of Cr was detected. The good agreement with the

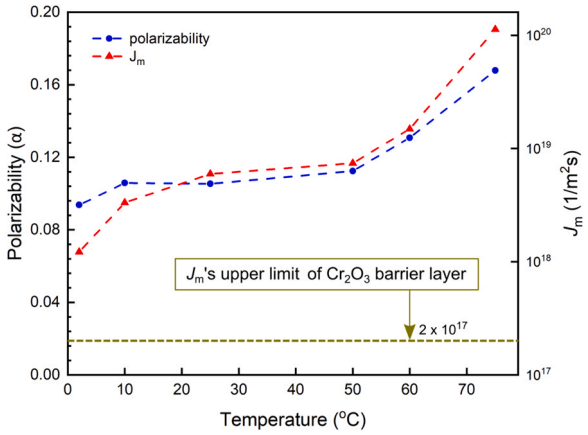

Fig. 13. Effect of temperature on the polarizability of the passive layer/solution interface (α) and the rate of annihilation of the cation vacancies at the metal/ film interface (J_m) for $Al_2Cr_5Cu_5Fe_{53}Ni_{35}$ alloys in seawater.

XPS results provides a convincing argument for the validity of the Point Defect Model.

Based on the values of polarizability (α) at the passive layer/solution interface and the rate of annihilation of the cation vacancies at the metal/film interface (J_m), the metal cation diffusivity at the metal barrier, D, can be obtained from the relationships presented in Eq. 8, 9 and 10. The polarizability was considered a weak function of the temperature when calculating the value of D [29,64]. The calculated cation vacancy diffusion coefficients D for the passive film formed by $Al_2Cr_5Cu_5Fe_{53}Ni_{35}$ alloys are shown in Fig. 14(a). According to the result shown in Fig. 14(a), the value of the metal cation vacancies diffusivity (D) increases with temperature, indicating that higher temperature will decrease the stability of the passive film formed on the $Al_2Cr_5Cu_5Fe_{53}Ni_{35}$ alloys in seawater, as observed in previous electrochemical experiments.

4.2. Evaluation of the solution temperature effect on the passive film

Figure 14 (a) also presents the pitting potential (E_p) and the potential difference between OCP and pitting potential (ΔE) in seawater solution under different temperatures. It can be observed from Fig. 14(a) that the values of E_p and ΔE are decreasing with the increasing value of D while the temperature of the solution rises, which indicates that not only the limits but also the stability of the passive film decrease with the increasing temperature. It is associated with the increasing of D within the passive film formed by the $Al_2Cr_5Cu_5Fe_{53}Ni_{35}$ alloy under the conditions above considered. This passive film behavior is consistent with the prediction of PDM analysis, as it can be seen in Eq. 8, the rising in the value of D will lower pitting potential by increasing the mobility of the cation vacancies at the metal/film interface. This is coherent with the explanation based on the presence of highly defective outer layer which is also pointed out in previous publications [60,65]. The ΔE has a significant drop between 25°C and 50°C, and also the slope of the D curve is steeper after 50°C, these results indicate the transition of passive to active is dictated by the consistency of the passive layer, which is in a good agreement with the EIS analysis.

4.3. Quantitative comparison with a conventional martensitic stainless steel

Many efforts have been made using PDM approach to evaluate the corrosion behavior of martensitic stainless steels [66–68,63]. UNS S40300 stainless steel in the borate buffer solution (pH = 8.1) [63] was chosen to compare with current high-entropy alloy. The reason is that the pH environment is an important factor in metal cation diffusivity [32] and the pH of the simulated seawater solution is about 7.9. With α and J_m values provided in the work [63], the metal cation diffusivity (D) of the UNS S40300 stainless steel can be calculated. The quantitative comparison results of D between the $Al_2Cr_5Cu_5Fe_{53}Ni_{35}$ alloy and UNS S40300 stainless steel are presented in Fig. 14(b). According to the results shown in Fig. 14(b), the value D of UNS S40300 is larger than the $Al_2Cr_5Cu_5Fe_{53}Ni_{35}$ alloy when the temperature lower than 60°C. Based on the physicochemical model underlying by PDM , it can be concluded that the passive film formed on the surface of the $Al_2Cr_5Cu_5Fe_{53}Ni_{35}$ alloy is more stable and superior than the UNS S40300 stainless steel when the temperature is not exceed more than 60°C in certain pH solutions. In general, high-entropy alloys usually have promising mechanical properties [69], therefore $Al_2Cr_5Cu_5Fe_{53}Ni_{35}$ alloy, based on the current analyses, may serve as starting point for the discovery of new corrosion resistant alloys that bring scientific significance and practical benefit.

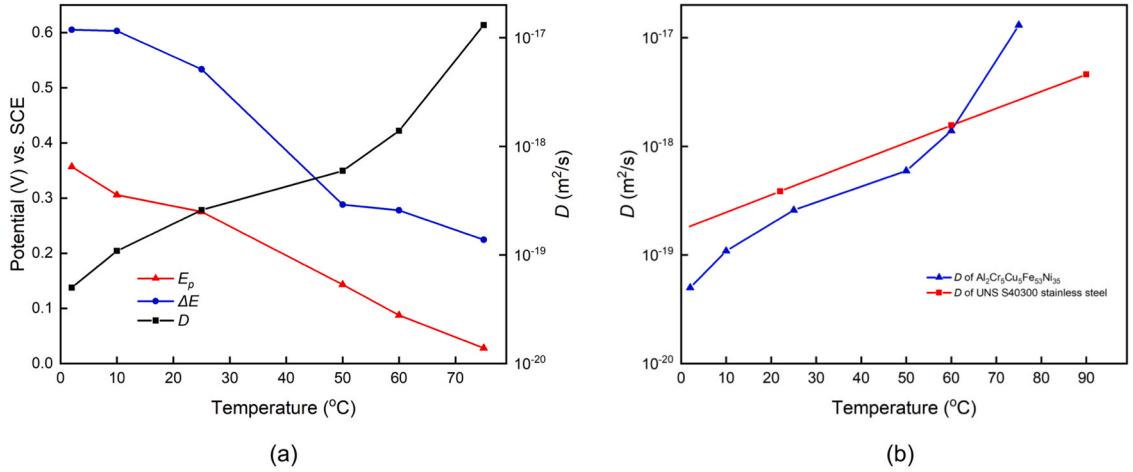

Fig. 14. (a) The pitting potential (E_p), potential difference between OCP and pitting potential (ΔE), and metal cation diffusivity (D) of $Al_2Cr_5Cu_5Fe_{53}Ni_{35}$ alloy in seawater at different temperatures; (b) The metal cation diffusivity (D) between $Al_2Cr_5Cu_5Fe_{53}Ni_{35}$ alloys and UNS S40300 stainless steel [63] in the solution with similar pH.

5. Conclusions

- The $Al_2Cr_5Cu_5Fe_{53}Ni_{35}$ is a single-phase, solid solution alloy with FCC crystal structure, similar to FeNi intermetallic compound. Owing to the different atom sizes of the constituent elements, XRD analysis indicates the presence of distorted crystalline lattice structure whose averaged grain size is about 500 μm.
- The potentiodynamic-polarization and potentiastatic staircase experiments show the localized corrosion resistance of $Al_2Cr_5Cu_5Fe_{53}Ni_{35}$ alloy is undermined by higher concentrations of chloride in the solvent. Likewise, the resistance to localized corrosion diminishes as solution temperature rises, especially in the range above 50°C where the alloy undergoes corrosion without transition stage between activation and passivation. These external factors (temperature and acidity) promote instability and subsequent passive film breakdown. Conversely, the impedance analysis indicates that the $Al_2Cr_5Cu_5Fe_{53}Ni_{35}$ alloy could spontaneously form a protective film at lower temperatures (2°C, 10°C, and 25°C) almost without active dissolution process at the working electrode surface.
- Stable passive film formation at room temperature is observed that is mainly comprised by Al_2O_3 surface layer with few micro porous-like defects, which can act as entrances of Cl^- anions into the metal surface. These pores can be exacerbated by higher temperatures making the apparent film thickness grows as indicated in Table 4, thereby facilitating film breakdown and active dissolution.
- The Point Defect Model (PDM) approach provides a convincing argument about the passive film properties of the $Al_2Cr_5Cu_5Fe_{53}Ni_{35}$ alloy formed in seawater solution. The values of polarizability (α), cation vacancies at the metal/film interface (J_m) and metal cation diffusivity at the metal barrier (D), all increase with the solution temperature indicating that higher temperature will decrease the stability of the passive film in seawater. According to the PDM analysis, the localized corrosion resistance of $Al_2Cr_5Cu_5Fe_{53}Ni_{35}$ alloy is slightly superior to UNS S40300 stainless steel when temperature is below 60°C.

Data Availability

Data will be made available on request.

Declaration of Competing Interest

The authors declare that they have no known competing financial interests or personal relationships that could have appeared to influence the work reported in this paper.

Acknowledgment

LX and MP would like to thank the National Corrosion and Materials Reliability Laboratory and the Ocean Engineering Department, both in TAMU, for allowing the use of their top-notch experimental facilities and providing research funds in the form of startup grant, respectively. Moreover, to the MIT Industrial Fracture Consortium for the partial funding received by virtue of this investigation is also acknowledge.

CRediT authorship contribution statement

L. Xue: Methodology, Formal analysis, Investigation, Validation, Writing – original draft. **Y. Ding:** Methodology. **K.G. Pradeep:** Conceptualization, Methodology, Investigation, Writing - review & editing. **R. Case:** Conceptualization, Methodology, Resources, Writing – review & editing. **H. Castaneda:** Resources, Writing – review & editing. **M. Paredes:** Conceptualization, Methodology, Investigation, Resources, Writing – original draft, Writing – review & editing, Supervision.

References

[1] B. Cantor, I.T. Chang, P. Knight, A.J. Vincent, Microstructural development in equiatomic multicomponent alloys (1-2 SPEC. ISS.), Mater. Sci. Eng. A (2022) 375–377, https://doi.org/10.1016/j.msea.2003.10.257 (1-2 SPEC. ISS.).
[2] J.W. Yeh, S.K. Chen, S.J. Lin, J.Y. Gan, T.S. Chin, T.T. Shun, C.H. Tsau, S.Y. Chang, Nanostructured high-entropy alloys with multiple principal elements: Novel alloy design concepts and outcomes, Adv. Eng. Mater. 6 (5) (2022), https://doi.org/10.1002/adem.200300567
[3] J.W. Yeh, S.K. Chen, J.Y. Gan, S.J. Lin, T.S. Chin, T.T. Shun, C.H. Tsau, S.Y. Chang, Formation of simple crystal structures in Cu-Co-Ni-Cr-Al-Fe-Ti-V alloys with multiprincipal metallic elements, Metall. Mater. Trans. A Phys. Metall. Mater. Sci. 35 A (8) (2022), https://doi.org/10.1007/s11661-006-0234-4
[4] T.K. Chen, M.S. Wong, T.T. Shun, J.W. Yeh, Nanostructured nitride films of multi-element high-entropy alloys by reactive DC sputtering, Surf. Coat. Technol. 200 (5–6) (2022), https://doi.org/10.1016/j.surfcoat.2005.08.081
[5] C.Y. Hsu, J.W. Yeh, S.K. Chen, T.T. Shun, Wear resistance and high-temperature compression strength of Fcc CuCoNiCrAl0.5Fe alloy with boron addition, Metall. Mater. Trans. A: Phys. Metall. Mater. Sci. 35 A (5) (2022), https://doi.org/10.1007/s11661-004-0254-x
[6] P.K. Huang, J.W. Yeh, T.T. Shun, S.K. Chen, Multi-principal-element alloys with improved oxidation and wear resistance for thermal spray coating, Adv. Eng. Mater. 6 (1–2) (2022), https://doi.org/10.1002/adem.200300507
[7] D.B. Miracle, O.N. Senkov critical review of high entropy alloys and related concepts(2017). 10.1016/j.actamat.2016.08.081.
[8] S.H. Shim, H. Pouraliakbar, S.I. Hong, High strength dual fcc phase CoCuFeMnNi high-entropy alloy wires with dislocation wall boundaries stabilized by phase boundaries, Mater. Sci. Eng. A 825 (2022), https://doi.org/10.1016/j.msea.2021.141875
[9] B. Gludovatz, A. Hohenwarter, K.V. Thurston, H. Bei, Z. Wu, E.P. George, R.O. Ritchie, Exceptional damage-tolerance of a medium-entropy alloy CrCoNi at cryogenic temperatures, Nat. Commun. 7 (2022), https://doi.org/10.1038/ncomms10602
[10] C. Niu, C.R. LaRosa, J. Miao, M.J. Mills, M. Ghazisaeidi, Magnetically-driven phase transformation strengthening in high entropy alloys, Nat. Commun. 9 (1) (2022), https://doi.org/10.1038/s41467-018-03846-0
[11] Z. Li, K.G. Pradeep, Y. Deng, D. Raabe, C.C. Tasan, Metastable high-entropy dual-phase alloys overcome the strength-ductility trade-off, Nature 534 (7606) (2022), https://doi.org/10.1038/nature17981
[12] D.B. Miracle High entropy alloys as a bold step forward in alloy development (2019). 10.1038/s41467–019-09700–1.
[13] Y. Zhang, T.T. Zuo, Z. Tang, M.C. Gao, K.A. Dahmen, P.K. Liaw, Z.P. Lu, Microstructures and properties of high-entropy alloys (2014). 10.1016/j.pmatsci.2013.10.001.
[14] C. Chen, S. Pang, Y. Cheng, T. Zhang, Microstructure and mechanical properties of Al20-xCr20.0.5xFe20Co20Ni20.0.5x high entropy alloys, J. Alloy. Compd. 659 (2022), https://doi.org/10.1016/j.jallcom.2015.10.258
[15] U. Roy, H. Roy, H. Daoud, U. Glatzel, K.K. Ray, Fracture toughness and fracture micromechanism in a cast AlCoCrCuFeNi high entropy alloy system, Mater. Lett. 132 (2022), https://doi.org/10.1016/j.matlet.2014.06.067
[16] Z. Tang, T. Yuan, C.W. Tsai, J.W. Yeh, C.D. Lundin, P.K. Liaw, Fatigue behavior of a wrought Al0.5CoCrCuFeNi two-phase high-entropy alloy, Acta Mater. 99 (2022), https://doi.org/10.1016/j.actamat.2015.07.004
[17] S.G. Ma, S.F. Zhang, M.C. Gao, P.K. Liaw, Y. Zhang, A successful synthesis of the CoCrFeNiAl0.3 single-crystal, high-entropy alloy by Bridgman solidification, JOM 65 (12) (2022), https://doi.org/10.1007/s11837-013-0733-x
[18] Y. Qiu, M.A. Gibson, H.L. Fraser, N. Birbilis, Corrosion characteristics of high entropy alloys, Mater. Sci. Technol. 31 (10) (2022), https://doi.org/10.1179/1743284715Y.0000000026
[19] Y.X. Liu, C.Q. Cheng, J.L. Shang, R. Wang, P. Li, J. Zhao, Oxidation behavior of high-entropy alloys AlxCoCrFeNi (x = 0.15, 0.4) in supercritical water and comparison with HR3C steel, Trans. Nonferrous Met. Soc. China 25 (4) (2022), https://doi.org/10.1016/S1003-6326(15)63733-5
[20] Y. Shi, B. Yang, X. Xie, J. Brechtl, K.A. Dahmen, P.K. Liaw, Corrosion of Al xCoCrFeNi high-entropy alloys: Al-content and potential scan-rate dependent pitting behavior, Corros. Sci. 119 (2022), https://doi.org/10.1016/j.corsci.2017.02.019
[21] Y. Shi, B. Yang, P.K. Liaw, Corrosion-resistant high-entropy alloys: A review (2017). 10.3390/met7020043.
[22] C. Ng, S. Guo, J. Luan, Q. Wang, J. Lu, S. Shi, C.T. Liu, Phase stability and tensile properties of Co-free Al 0.5CrCuFeNi2 high-entropy alloys, J. Alloy. Compd. 584 (2022), https://doi.org/10.1016/j.jallcom.2013.09.105
[23] S. Guo, C. Ng, C.T. Liu, Anomalous solidification microstructures in Co-free Al xCrCuFeNi2 high-entropy alloys (2013). 10.1016/j.jallcom.2013.01.007.
[24] S.S. Nene, M. Frank, K. Liu, S. Sinha, R.S. Mishra, B.A. McWilliams, K.C. Cho, Corrosion-resistant high entropy alloy with high strength and ductility, Scr. Mater. 166 (2022), https://doi.org/10.1016/j.scriptamat.2019.03.028
[25] B. Gwalani, D. Choudhuri, V. Soni, Y. Ren, M. Styles, J.Y. Hwang, S.J. Nam, H. Ryu, S.H. Hong, R. Banerjee, Cu assisted stabilization and nucleation of L12

precipitates in Al0.3CuFeCrNi2 fcc-based high entropy alloy, Acta Mater. 129 (2017) 170–182, https://doi.org/10.1016/J.ACTAMAT.2017.02.053
[26] Z. Cvijović, G. Radenković, Microstructure and pitting corrosion resistance of annealed duplex stainless steel, Corros. Sci. 48 (12) (2022), https://doi.org/10.1016/j.corsci.2006.04.003
[27] J.O. Nilsson, A. Wilson, Influence of isothermal phase transformations on toughness and pitting corrosion of super duplex stainless steel SAF 2507, Mater. Sci. Technol. 9 (7) (2022), https://doi.org/10.1179/026708393790172222
[28] N.D. Budiansky, L. Organ, J.L. Hudson, J.R. Scully, Detection of interactions among localized pitting sites on stainless steel using spatial statistics, J. Electrochem. Soc. 152 (4) (2022), https://doi.org/10.1149/1.1869192
[29] R. Case, Evaluation of the passivity limits in austenitic stainless steel exposed to H2S-containing brines using point defect model analysis, Corros. Eng., Sci. Technol. (2021) 1–14.
[30] Y. Zhang, D.D. Macdonald, M. Urquidi-Macdonald, G.R. Engelhardt, R.B. Dooley, Passivity breakdown on AISI Type 403 stainless steel in chloride-containing borate buffer solution, Corros. Sci. 48 (11) (2022), https://doi.org/10.1016/j.corsci.2006.01.009
[31] J. Zhong, F. Mao, E. Ghanbari, D.D. Macdonald, Passivity breakdown on 300 M and S280 ultra-high strength steels in borate buffer solutions containing chloride ion, Electrochim. Acta 251 (2022), https://doi.org/10.1016/j.electacta.2017.08.116
[32] S. Yang, D.D. Macdonald, Theoretical and experimental studies of the pitting of type 316L stainless steel in borate buffer solution containing nitrate ion, Electrochim. Acta 52 (5) (2022), https://doi.org/10.1016/j.electacta.2006.07.052
[33] A. International, International, D1141-98 standard practice for the preparation of substitute ocean water (Reapproved), ASTM Int. 98 (2013) (Reapproved).
[34] R. Srinivasan, F. Fasmin, An Introduction to Electrochemical Impedance Spectroscopy, 2021.10.1201/9781003127932.
[35] C.H. Cheng, J. Ning, R. Case, Development of a reference electrode for study of supercritical CO2 corrosion, in: NACE - International Corrosion Conference Series, vol. 2018-April, 2018.
[36] ASTM-Standards, Standard practice for calculation of corrosion rates and related information from electrochemical measurements, ASTM G 102–89(Reapproved). 2022.
[37] T. Haruna, D.D. Macdonald, Theoretical prediction of the scan rate dependencies of the pitting potential and the probability distribution in the induction time, J. Electrochem. Soc. 144 (5) (2022), https://doi.org/10.1149/1.1837643
[38] D.D. Macdonald, Passivity - The key to our metals-based civilization, Pure Appl. Chem. 71 (6) (2022), https://doi.org/10.1351/pac199971060951
[39] E. Barsoukov, J.R. Macdonald, Impedance Spectroscopy: Theory, Experiment, and Applications, 2005.10.1002/0471716243.
[40] P. Bommersbach, C. Alemany-Dumont, J.P. Millet, B. Normand, Formation and behaviour study of an environment-friendly corrosion inhibitor by electrochemical methods, Electrochim. Acta 51 (6) (2022), https://doi.org/10.1016/j.electacta.2005.06.001
[41] K. Es-Salah, M. Keddam, K. Rahmouni, A. Srhiri, H. Takenouti, Aminotriazole as corrosion inhibitor of Cu-30Ni alloy in 3% NACl in presence of ammoniac, Electrochim. Acta 49 (17–18) (2004) 2771–2778, https://doi.org/10.1016/j.electacta.2004.01.038 ⟨https://linkinghub.elsevier.com/retrieve/pii/S0013468604002440⟩.
[42] H. Zhang, Y. Zhao, Z. Jiang, Effects of temperature on the corrosion behavior of 13Cr martensitic stainless steel during exposure to CO_2 and Cl- environment, Mater. Lett. 59 (27) (2005) 3370–3374, https://doi.org/10.1016/j.matlet.2005.06.002 ⟨https://linkinghub.elsevier.com/retrieve/pii/S0167577×05005598⟩.
[43] A.C. Bastos, M.G. Ferreira, A.M. Simões, Corrosion inhibition by chromate and phosphate extracts for iron substrates studied by EIS and SVET, Corros. Sci. 48 (6) (2022), https://doi.org/10.1016/j.corsci.2005.05.021
[44] Y.B. Hu, C.F. Dong, M. Sun, K. Xiao, P. Zhong, X.G. Li, Effects of solution pH and Cl-on electrochemical behaviour of an Aermet100 ultra-high strength steel in acidic environments, Corros. Sci. 53 (12) (2022), https://doi.org/10.1016/j.corsci.2011.08.024
[45] M.P. Ryan, D.E. Williams, R.J. Chater, B.M. Hutton, D.S. McPhail, Why stainless steel corrodes, Nature 415(6873). 2022.10.1038/415770a.
[46] B. Hirschorn, M.E. Orazem, B. Tribollet, V. Vivier, I. Frateur, M. Musiani, Determination of effective capacitance and film thickness from constant-phase-element parameters, Electrochim. Acta 55 (21) (2022), https://doi.org/10.1016/j.electacta.2009.10.065
[47] J.R. Macdonald, Impedance spectroscopy and its use in analyzing the steady-state AC response of solid and liquid electrolytes, J. Electroanal. Chem. 223 (1–2) (2022), https://doi.org/10.1016/0022-0728(87)85249-X
[48] C.H. Hsu, F. Mansfeld, Concernng the conversion of the constant phase element parameter Y0 into a capacitance, Corrosion 57 (9) (2022), https://doi.org/10.5006/1.3280607
[49] S.P. Harrington, T.M. Devine, Relation between the semiconducting properties of a passive film and reduction reaction rates, J. Electrochem. Soc. 156 (4) (2022), https://doi.org/10.1149/1.3077576
[50] Y. Sun, A. Lan, M. Zhang, H. Yang, J. Qiao, Influence of lanthanum on passivity behavior of CrMnFeNi high entropy alloys, Mater. Chem. Phys. 265 (2022), https://doi.org/10.1016/j.matchemphys.2021.124509
[51] M.G.S. Ferreira, J.L. Dawson, Electrochemical studies of the passive film on 316 stainless steel in chloride media, J. Electrochem. Soc. 132 (4) (2022), https://doi.org/10.1149/1.2113954
[52] A. Barrera, F. Tzompantzi, J. Campa-Molina, J.E. Casillas, R. Pérez-Hernández, S. Ulloa-Godinez, C. Velásquez, J. Arenas-Alatorre, Photocatalytic activity of Ag/Al2O3-Gd2O3 photocatalysts prepared by the sol-gel method in the degradation of 4-chlorophenol, RSC Adv. 8 (6) (2022), https://doi.org/10.1039/c7ra12665d
[53] M.C. Biesinger, B.P. Payne, A.P. Grosvenor, L.W. Lau, A.R. Gerson, R.S.C. Smart, Resolving surface chemical states in XPS analysis of first row transition metals, oxides and hydroxides: Cr, Mn, Fe, Co and Ni, Appl. Surf. Sci. 257 (7) (2022), https://doi.org/10.1016/j.apsusc.2010.10.051
[54] M.C. Biesinger, L.W. Lau, A.R. Gerson, R.S.C. Smart, Resolving surface chemical states in XPS analysis of first row transition metals, oxides and hydroxides: Sc, Ti, V, Cu and Zn, Appl. Surf. Sci. 257 (3) (2022), https://doi.org/10.1016/j.apsusc.2010.07.086
[55] B. Díaz, E. Härkönen, J. Światowska, V. Maurice, A. Seyeux, P. Marcus, M. Ritala, Low-temperature atomic layer deposition of Al2O3 thin coatings for corrosion protection of steel: surface and electrochemical analysis, Corros. Sci. 53 (6) (2022), https://doi.org/10.1016/j.corsci.2011.02.036
[56] A.M. Sadoun, M.M. Mohammed, E.M. Elsayed, A.F. Meselhy, O.A. El-Kady, Effect of nano Al2O3 coated Ag addition on the corrosion resistance and electrochemical behavior of Cu-Al2O3 nanocomposites, J. Mater. Res. Technol. 9 (3) (2022), https://doi.org/10.1016/j.jmrt.2020.02.076
[57] Digby D. Macdonald, J. Electrochem. Soc. 139 (1992) 3434, https://doi.org/10.1149/1.2069096
[58] D.D. Macdonald, X. Lei, Theoretical interpretation of anion size effects in passivity breakdown, J. Electrochem. Soc. 163 (13) (2022), https://doi.org/10.1149/2.0571613jes
[59] P. Lu, G.R. Engelhardt, B. Kursten, D.D. Macdonald, The kinetics of nucleation of metastable pits on metal surfaces: the point defect model and its optimization on data obtained on stainless steel, carbon steel, iron, aluminum and alloy-22, J. Electrochem. Soc. 163 (5) (2022), https://doi.org/10.1149/2.0401605jes
[60] J.-S. Lee, Y. Kitagawa, T. Nakanishi, Y. Hasegawa, K. Fushimi, Effect of hydrogen sulfide ions on the passive behavior of type 316L stainless steel, J. Electrochem. Soc. 162 (14) (2022), https://doi.org/10.1149/2.0861512jes
[61] T. Shibata, T. Takeyama, Stochastic theory of pitting corrosion, Corrosion 33 (7) (2022), https://doi.org/10.5006/0010-9312-33.7.243
[62] L. Bertolini, F. Bolzoni, T. Pastore, P. Pedeferri, Behaviour of stainless steel in simulated concrete pore solution, Br. Corros. J. 31 (3) (2022), https://doi.org/10.1179/bcj.1996.31.3.218
[63] Y. Zhang, M. Urquidi-MacDonald, G.R. Engelhardt, D.D. MacDonald, Development of localized corrosion damage on low pressure turbine disks and blades: II. Passivity breakdown, Electrochim. Acta 69 (2022), https://doi.org/10.1016/j.electacta.2012.01.023
[64] G.R. Engelhardt, R.P. Case, D.D. Macdonald, Electrochemical impedance spectroscopy optimization on passive metals, J. Electrochem. Soc. 163 (8) (2022), https://doi.org/10.1149/2.0811608jes
[65] Z. Wang, Z. Feng, L. Zhang, Effect of high temperature on the corrosion behavior and passive film composition of 316 L stainless steel in high H2S-containing environments, Corros. Sci. 174 (2022), https://doi.org/10.1016/j.corsci.2020.108844
[66] A. Fattah-alhosseini, F. Soltani, F. Shirsalimi, B. Ezadi, N. Attarzadeh, The semiconducting properties of passive films formed on AISI 316 L and AISI 321 stainless steels: A test of the point defect model (PDM), Corros. Sci. 53 (10) (2022), https://doi.org/10.1016/j.corsci.2011.05.063
[67] A. Fattah-alhosseini, Passivity of AISI 321 stainless steel in 0.5 MH2SO4 solution studied by Mott-Schottky analysis in conjunction with the point defect model, Arab. J. Chem. 9 (2022), https://doi.org/10.1016/j.arabjc.2012.02.015
[68] J. Geringer, D.D. MacDonald, Modeling fretting-corrosion wear of 316L SS against poly(methyl methacrylate) with the Point Defect Model: Fundamental theory, assessment, and outlook, Electrochim. Acta 79 (2022), https://doi.org/10.1016/j.electacta.2012.06.028
[69] E.P. George, W.A. Curtin, C.C. Tasan, High entropy alloys: A focused review of mechanical properties and deformation mechanisms (2020). 10.1016/j.actamat.2019.12.015.